A luminescence spectroscopy study of new Li2BaAl2F10 single crystal

Article *in* Optical Materials · February 2018

DOI: 10.1016/j.optmat.2017.12.017

6 authors, including:

V.A. Pustovarov
Ural Federal University
315 PUBLICATIONS **1,251** CITATIONS
SEE PROFILE

Igor N. Ogorodnikov
Ural Federal University
206 PUBLICATIONS **999** CITATIONS
SEE PROFILE

L. I. Isaenko
Sobolev Institute of Geology and Mineralogy
305 PUBLICATIONS **3,033** CITATIONS
SEE PROFILE

Alina Goloshumova
Sobolev Institute of Geology and Mineralogy
17 PUBLICATIONS **73** CITATIONS
SEE PROFILE

Optical Materials. V.76 (February 2018). P.1–10. DOI: 10.1016/j.optmat.2017.12.017

A luminescence spectroscopy study of new $Li_2BaAl_2F_{10}$ single crystal

V. A. Pustovarov[a], I. N. Ogorodnikov[a,*], L. I. Isaenko[b,c], S. I. Lobanov[c], A. A. Goloshumova[c], D. Yu. Naumov[d]

[a] *Ural Federal University, 19, Mira Street, 620002 Yekaterinburg, Russia*
[b] *Novosibirsk State University, 2, Pirogova Street, 630090 Novosibirsk, Russia*
[c] *V. S. Sobolev Institute of Geology and Mineralogy SB RAS, ac. Koptyug Avenue, 3, 630090 Novosibirsk, Russia*
[d] *A. V. Nikolaev Institute of Inorganic Chemistry SB RAS, ac. Lavrentiev Avenue, 3, 630090 Novosibirsk, Russia*

Abstract

Large $Li_2BaAl_2F_{10}$ single crystals of optical quality were grown using the vertical Bridgman method. X-ray diffraction method was used to determine the crystal structure (orthorhombic symmetry $Cmc2_1$), lattice parameters, atomic coordinates. The luminescent properties were investigated using selective photoexcitation by synchrotron radiation ($E = 3.7$–21 eV, $T = 8$ K, time integrated and time-resolved spectra) as well as upon excitation with unfiltered X-ray beam (synchrotron radiation or X-ray tube). We revealed both the broadband luminescence at $E_m = 4.0$ eV (E_{ex}=11.72 eV) attributed to the radiative annihilation of self-trapped excitons (STE) and the excitonic-type near-defect luminescence at $E_m = 3.0$–3.2 eV (E_{ex}=11.25 eV) attributed to radiative relaxation of electronic excitations in nonequivalent structural units of the crystal lattice. The fast exponential component with lifetime of 5.6 ns, a low-intensity intermediate component with a lifetime of 75–100 ns, a constant level — pedestal (sum of the micro- and millisecond decay components) were revealed in luminescence decay kinetics. The electronic structure parameters (bandgap $E_g = 13.0$ eV, low-energy onset of the intrinsic host absorption $E_c = 11.2$ eV), the energy threshold for the excitation of STE-luminescence ($E_{th} = 11.2$ eV) are determined from spectroscopic data. Thermoluminescence (TL) has been studied (90–350 K) using spectral-integral regime. Four partially overlapping TL glow peaks were revealed, their deconvolution was done and thermal activation parameters were determined using TGCD method.

Keywords:
decafluoride $Li_2BaAl_2F_{10}$, vertical Bridgman method, crystallographic structure, electronic structure parameters, luminescence spectra, thermoluminescence

1. Introduction

Complex fluorides and double fluorine salts have many practical applications as optical materials [1]. From simple fluorides, they inherited a wide band of optical transparency, extending far into the vacuum ultraviolet (VUV) spectral region. For example, LiF has a band width $E_g = 13.6$ eV [2]. The latter is especially important, because of continuously increasing need in compact laser sources of VUV-UV energy region for such applications as photolithography, analytical instrumentations, medicine, and many others [3, 4]. However, in addition to this parameter, it is necessary to take into account other characteristics of the optical material. The continuous search for new complex compounds is aimed at providing the best balance between a large set of different characteristics. In addition to the obvious technological and economic parameters associated with the production of an optical material, this includes the possibility of doping with impurities that create efficient luminescent centers, the value of the isomorphous capacitance for substitutional impurities, the presence of an efficient transport of the energy of electronic excitations from the host lattice to the impurity centers, and many other physical and chemical characteristics.

The Li–Ba compounds are also of particular interest for radiation detection because the ^{6}Li-isotope has advantages in interaction with thermal neutrons. There are two more crucial reasons. First, the Ba^{2+} ion is responsible for core-valence transitions F^- $2p \rightarrow Ba^{2+}$ $5p$ (so called 'Auger-free luminescence'), which features subnanosecond decay times. Second, a fluorine compound as a whole exhibits self-trapped exciton (STE) luminescence, which is not manifested under thermal-neutron irradiation. As both emissions give a response under gamma-ray excitation, this offer a unique opportunity for thermal neutron — gamma discrimination [5]. Some important impurities were also tested as luminescence centers for $LiBaF_3$ (Eu^{2+} [6] and Pb^+ [7, 8]).

Fluoride crystals based on triple fluorine salts with common formula $Li\,Me\,AlF_6$ (Me = Ca, Sr, Ba) are traditionally used in laser technology as optical materials operating in the UV–VUV spectral ranges. In this regard, their optical and electronic structure properties are the subject of intensive research. The $LiCaAlF_6$ and $LiSrAlF_6$ crystals have been studied in sufficient detail [9–11], but $LiBaAlF_6$ (LBAF) crystals have attracted less attention. Luminescence and optical properties of undoped LBAF single crystals are reported in [12, 13]. The band gap

*Corresponding author
Email address: i.n.ogorodnikov@urfu.ru (I. N. Ogorodnikov)

E_g was estimated as 12.1 eV in [12] and updated to more accurate value of 12.3 eV in [14]. Both the cross-luminescence and intra-band luminescence of LBAF were reported in [12, 13]. The luminescence spectroscopy of Pr^{3+}-doped LBAF crystals was previously reported in [15]. Effect of an electron beam irradiation on optical and luminescence properties of $LiBaAlF_6$ crystals has been studied in [16]. VUV-luminescence of monoclinic Li_3AlF_6 single crystals has been studied in [17, 18].

The search for noncentrosymmetric optical crystals operating in the VUV spectral range led to the synthesis of the new compound $Li_2BaAl_2F_{10}$ (LBAF10). In the present work, large LBAF10 single crystals have been grown and their crystallographic and luminescence properties have been studied. The purpose of this experimental work was to obtain a set of primary data relating to the crystallographic structure of LBAF10, to study their luminescence properties and to determine the electronic structure parameters. It should be specially emphasized that in this experimental work we did not plan to carry out any theoretical studies, for example, quantum-chemical calculations of the electronic structure. Such calculations require a separate special study.

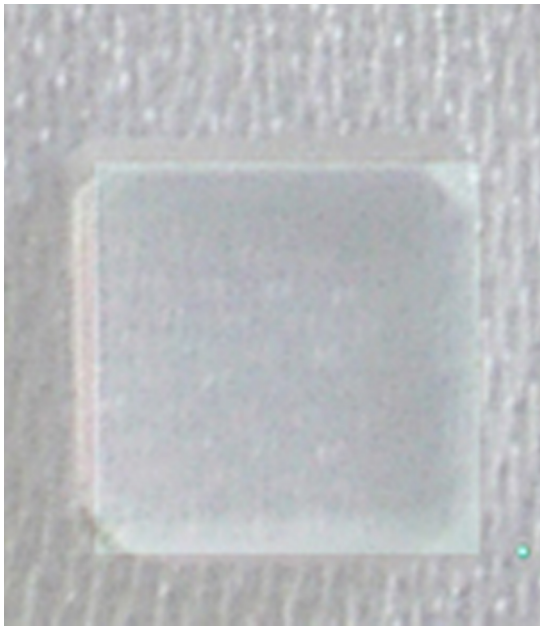

Figure 1: Sample of LBAF10 crystal used in research work. The sample 3×3×1.5 mm^3 in size was cut from single-crystal part of ingot.

2. Experimental details

Binary LiF, BaF_2 and AlF_3 were used as initial materials to synthesize LBAF10 compound. Powders of fluorides taken in stoichiometric ratio were being annealed for 5 hours at $T = 120\,^{\circ}C$ and then filled in a glass-graphite crucible, which was set in a quartz ampoule. It was being evacuated on the vacuum post for 5 hours at 150 °C and then sealed. To homogenize the mixture the ampoule was being rotated at the temperature up to 1200 °C for 1 hour. The LBAF10 crystals were grown by the vertical Bridgman method in a two-zone furnace. The temperature in the hot zone was 900 °C, which is 150 °C above the melting point of the compound, and the temperature of the cold zone was 500 °C. The ampoule was moved from the hot zone into the cold one with a speed of 5 mm/day. The vertical temperature gradient in crystallization zone was 20 °C/cm. As a result a polycrystalline ingot with individual single crystals up to 5×5×5 mm^3 in size was obtained, Fig. 1.

The luminescence study was performed using several experimental facilities, the parameters and capabilities of which are complementary.

Experimental setup #1. The photoluminescence (PL) emission spectra in the energy range of 1.2–6.21 eV, PL excitation (PLE) spectra (3.7–21 eV) were measured with selective photoexcitation by synchrotron radiation (SR) at the experimental station SUPERLUMI [19] (DESY, Hamburg). The SR pulses of the DORIS storage ring had a Gaussian shape (FWHM = 130 ps) with a repetition period of 96 ns. The measurements were carried out both in time-integrated (TI) and time-windowed modes at $T = 8$ K using an ultra-high-vacuum cryostat with a pressure of residual gases lower than 5×10^{-8} Pa. A 2 m-vacuum monochromator equipped with an Al-coated diffraction grating (spectral resolution 0.32 nm) was used for selective PL excitation. The PL excitation spectra are normalized to an equal number of photons incident on the sample. The PL emission spectra were recorded using the 0.3 m Spectra Pro-308i ARC monochromator and cooled CCD camera. PL emission spectra were normalized to spectral sensitivity of recording system. Time-resolved PLE-spectra were recorded using a R6358P (Hamamatsu)-type photomultiplier tube (PMT) in two independent time windows (TW) synchronized with respect to the excitation pulse beginning: 1.8–10.4 ns (TW1) and 36–66 ns (TW2). The parameters of the time-windows were chosen based on the PL decay kinetics.

Experimental setup #2. These measurements were performed in the laboratory of Solid state physics (Ural Federal University, Yekaterinburg, Russia). The emission spectra (1.5–5.8 eV) of steady-state luminescence upon an X-rays excitation (the steady-state X-ray induced luminescence, XRL) were recorded at two different temperatures $T = 90$ and 293 K upon excitation by unfiltered X-ray beam from the X-ray tube (BSW2:Cu, $U_a = 40$ kV and $I_a = 10$ mA). A MDR-23 grating monochromator (diffraction grating of 1200 lines/mm, inverse linear dispersion of 1 nm/mm) and a FEU-106 type PMT operating in the photon counting mode were used as recording system. The thermoluminescence (TL) glow curves were recorded in a spectral-integral regime using a FEU-39 PMT (2.0–6.2 eV). Heating rate was 0.3 K/s.

Experimental setup #3. These measurements were carried out by the use of the time-resolved luminescence station based on the SR-channel of the VEPP-3 storage ring (Budker Institute of Nuclear Physics, Novosibirsk, Russia). The energy of exciting photons was 3–60 keV. The spectral and kinetic measurements of luminescence were made through the electronic and optical chronography techniques based on the LI-602 type dissector with the operating spectral range of 1.5–6 eV [20]. Parameters of the luminescence time-response were determined on the assumption that the experimental time-

Table 1: Crystallographic data and structure refinement for $Li_2BaAl_2F_{10}$

Parameter	Description
Empirical formula	$Al_2\,Ba\,F_{10}\,Li_2$
Molecular weight	395.18
Temperature, K	150(2)
Wavelength, Å	0.71073
Crystal system	Orthorhombic
Space group	$Cmc2_1$
Lattice parameters, Å	$a = 5.2380(2)$ $\alpha = 90^\circ$
	$b = 18.4993(8)$ $\beta = 90^\circ$
	$c = 7.0518(3)$ $\gamma = 90^\circ$
Unit cell volume, Å^3	683.31(5)
Number of formula units per unit cell Z	4
Density (calculated)	3.841 g/cm^3
Crystal size	0.08×0.07×0.04 mm^3
Theta range for data collection	from 2.20 to 28.27 °
Reflections collected	2594
Independent reflections	933 [R(int) = 0.0260]
Absorption correction	Semi-empirical from equivalents
Refinement method	Full-matrix least-squares on F^2
Goodness-of-fit on F^2	0.916
Final R indices [$I > 2\sigma(I)$]	R1 = 0.0114, wR2 = 0.0262
R indices (all data)	R1 = 0.0114, wR2 = 0.0262
Absolute structure parameter	0.135(12)
Extinction coefficient	0.0031(2)
Maximum and minimum residual electron densities	0.513 and −0.681 e/Å^3

Note. Parameters are presented in accordance with [22]: $F = f(h,k,l,x_c,y_c,z_c)$ is a structure factor (F_0 is the experimental factor, F_c is the calculated factor); h, k, l are Miller indices; x_c, y_c, z_c are atom position coordinates; $R_{int} = \sum |F_0^2 - \langle F_c^2 \rangle| / \sum F_0^2$, where $\langle F_c^2 \rangle$ is the average of all the measured equivalents; I is the intensity of the peaks; $\sigma(I)$ is the variance of the intensity; R-factor (residual factor) characterizes the accuracy of the performed investigation, three variants of it were used: $S = \left[\sum |w\,(F_0^2 - F_c^2)^2| / (N_r - N_p)\right]^{1/2}$, where N_r is the number of unique reflections, N_p is the number of refined parameters, w is the weighting factor; $R1 = \sum ||F_0| - |F_c|| \,/\, \sum |F_0|$; $wR2 = \left[\sum w\,(F_0^2 - F_c^2)^2 / \sum w\,F_0^2\right]^{1/2}$.

response resulted from convolution of the luminescence decay kinetics proper and the excitation pulse profile (Gaussian shape, $\sigma = 430$ ps, the excitation pulse rate was 4 MHz). The storage ring current was usually about 100 mA. This corresponds to $3{\times}10^{16}$ photons cm^{-2} s^{-1}. Luminescence spectra were corrected taking into account the spectral dependence of the recording system.

3. Experimental results

3.1. Crystallographic structure of LBAF10

Clean and optically transparent sample was used for single crystal XRD experiment. Single crystal data were collected with the Mo K_α-radiation using a Bruker APEX DUO diffractometer equipped with a graphite monochromator. The measurement conditions are shown in Tab. 1. The collected experimental data were processed using SHELXTL software {Bruker AXS Inc. (2004), APEX (Version 1.08), SAINT (Version 7.03), SADABS (Version 2.11) and SHELXTL (Version 6.12) Bruker Advanced X-Ray Solutionse Madison, Wisconsin, USA}. Coordination numbers of cations in studied structures were defined by the Dirichlet polyhedra method using the *X*shell software [21]. For graphic visualization the BS program (Balls&Sticks ver. 1.42 by Sung J. Kang&Tadashi C. Ozawa) was used. Results of the experimental data processing and structure refinement are summarized in two tables: Tab. 1 shows the main crystallographic data, Tab. 2 shows the atomic coordinates and equivalent isotropic displacement parameters.

From our results (Tabs. 1 and 2) it follows that LBAF10 crystal has orthorhombic symmetry $Cmc2_1$ with the lattice parameters a= 5.2380(2) Å, b= 18.4993(8) Å, c= 7.0518(3) Å and atomic coordinates shown in Tab. 2. Barium ions occupy one nonequivalent position in crystal lattice, whereas lithium and aluminium ions both have two nonequivalent positions. Coordination number of Ba^{2+} is 8, and its coordination polyhedron is bicapped trigonal prism. Al^{3+} and $Li1^+$ are situated in octahedra, while coordination number for $Li2^+$ is 5 and its coordination polyhedron is a distorted tetragonal pyramid (Fig. 2). One can note that lithium polyhedra are rather distorted and cations deviate from their centers. Thus, for F6–F6–F5–F5 plane in Li1F6 the average bond distance value is 2.2095 Å, and the deviation of Li–F6 and Li–F5 bonds is 0.2525 Å (Fig.2, *c*, *d*). This compares to aluminium octahedra, where the difference between the average bond length and the longest and the shortest ones is an order of magnitude lower than that in Li1F6 (for example, 0.2525 Å in Li1F6 against 0.036 and 0.084 Å in

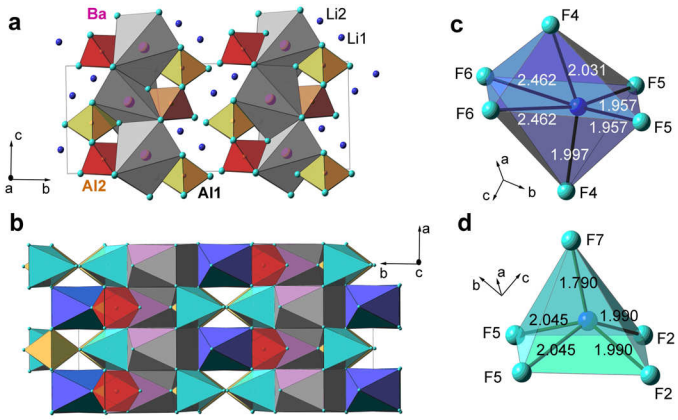

Figure 2: Crystallographic structure of $Li_2BaAl_2F_{10}$ along [100] (*a*) and [001] (*b*), coordination polyhedra of Li1 (*c*) and Li2 (*d*).

Al1F6). Moreover, for Li1-polyhedron the angle F4–Li1–F4 is 154.012°. In Li2F5 the angles F7–Li2–F5 and F7–Li2–F2 differ by 19.327° (101.019° and 120.346°, respectively). This is an important factor for nonlinear material as the distortion of structure units impacts nonlinear coefficients.

LBAF10 crystal structure is a frame of vertex-sharing cation polyhedra, where $Li1F_6$ octahedra have common facets with Al_2F_6 and shared edges with BaF_8; $Li2F_5$ have common facets with Ba and Al1 polyhedra.

Table 2: Atomic coordinates ($\times 10^4$) and equivalent isotropic displacement parameters ($0.001 Å^2$) for $Li_2BaAl_2F_{10}$. Parameter U_{eq} is defined as one third of the trace of the orthogonalized U^{ij} tensor

Atom	*x*	*y*	*z*	*U*(eq)
Ba(1)	0	2222(1)	6529(1)	5(1)
Al(1)	0	4123(1)	9611(2)	4(1)
Al(2)	0	1291(1)	11284(2)	5(1)
F(1)	0	3146(1)	9545(3)	10(1)
F(2)	−2437(2)	1670(1)	9786(2)	7(1)
F(3)	0	2098(1)	12692(3)	8(1)
F(4)	0	466(1)	9993(3)	7(1)
F(5)	2380(2)	4079(1)	11476(3)	7(1)
F(6)	2560(2)	4108(1)	7817(2)	10(1)
F(7)	0	5055(1)	9538(3)	9(1)
Li(1)	5000	4776(3)	12233(8)	11(1)
Li(2)	0	5977(4)	8770(11)	11(2)

Symmetry transformations used to generate equivalent atoms:

1. $x, y, z-1$;
2. $x+1/2, -y+1/2, z-1/2$;
3. $-x-1/2, -y+1/2, z-1/2$;
4. $x-1/2, -y+1/2, z-1/2$;
5. $-x+1/2, -y+1/2, z-1/2$;
6. $-x, y, z$;
7. $-x-1/2, -y+1/2, z+1/2$;
8. $-x+1/2, -y+1/2, z+1/2$;
9. $x-1/2, -y+1/2, z+1/2$;
10. $x-1/2, y-1/2, z$;
11. $x, y, z+1$;
12. $-x+1/2, y-1/2, z$;
13. $x, -y+1, z+1/2$;
14. $-x+1, -y+1, z-1/2$;
15. $-x+1, y, z$;
16. $x+1/2, y+1/2, z$;
17. $-x+1, -y+1, z+1/2$;
18. $-x-1/2, y+1/2, z$;
19. $-x, -y+1, z-1/2$;
20. $x, -y+1, z-1/2$;
21. $x-1/2, y+1/2, z$.

3.2. PL and PLE Spectra

PL under VUV excitation was studied using the experimental setup #1. Figure 3 shows PL emission spectra of LBAF10 crystal at $T = 8$ K recorded upon excitation at $E_{ex} = 13.0$ and 18.3 eV. These spectra are normalized to unity at the maximum intensity. In general, the PL emission spectra look practically identical: a common feature of both spectra is the dominant broad band at 4.0 eV (FWHM ≈ 1.4 eV) and the shoulder in the energy region of 2.5–3.0 eV. However, the shape of the difference spectrum indicates the probable presence of three more low-intensity bands at 2.8, 3.6, and 4.5 eV, Fig. 3, *b*.

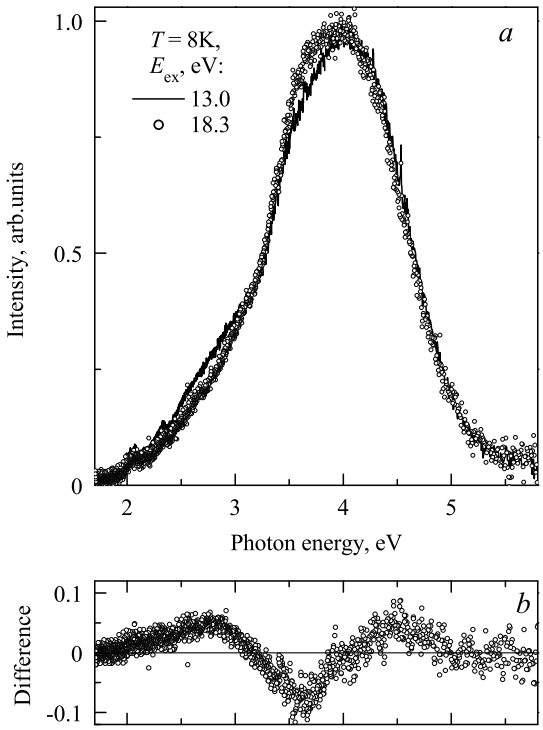

Figure 3: Panel *a*: Normalized PL emission spectra of LBAF10 crystal at $T = 8$ K recorded upon excitation at $E_{ex} = 13$ and 18.3 eV. Panel *b* shows difference between these spectra.

Figure 4 shows PLE spectra (time-integrated, TI; time-resolved, TW1 and TW2) for LBAF10 crystal at $T = 8$ K recorded monitoring emission at $E_m = 3.1$ and 3.9 eV. Each spectrum presented is normalized to the maximum intensity. Roman numerals with arrows indicate some PLE-peaks, discussed in the text. The relatively narrow (FWHM = 0.42 eV) PLE-peak (III) at 11.25 eV dominates all the spectra. The amplitude of the PLE peak (III) is taken as unity ($A_{III} = 1$) when the PLE spectrum is normalized in intensity. Another characteristic PLE-peak (IV) is located at 11.72 eV (the distance between the peaks $\Delta_{III-IV} = 0.47$ eV). Its amplitude depends on E_m. For $E_m = 3.1$ eV $A_{IV} = 1$, whereas for $E_m = 3.9$ eV, the dependence of the amplitude A_{IV} on the spectrum type is observed: $A_{IV} = 0.52$ (TI), 0.57 (TW2) and 0.59 (TW1). With a further increase in the excitation energy E_{ex}, a local minimum is observed at 12.9 eV, followed by an increase in the PLE intensity in the energy region at 13.4 eV (V). For $E_m = 3.1$ eV the amplitude of the peak is $A_V = 0.43$, then there is a plateau and

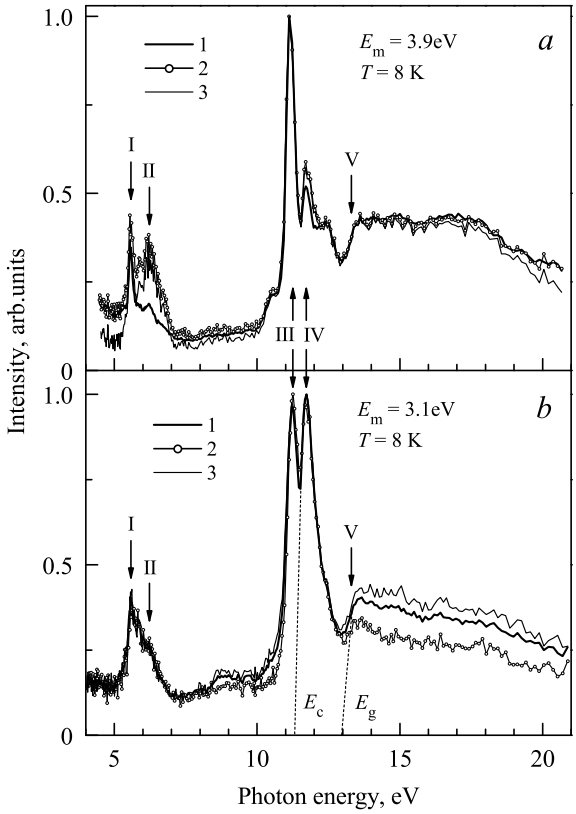

Figure 4: Time-integrated – (1) and time-resolved PLE spectra recorded in time-windows TW1 – (2) and TW2 – (3) monitoring emission at $E_m = 3.1$ and 3.9 eV for LBAF10 crystal at $T = 8$ K. The Roman numeral labeled arrows specify certain PLE peaks.

a small smooth decline in PLE-intensity in the energy region of 18–21 eV. For $E_m = 3.9$ eV, the peak amplitude A_V depends on the type of the spectrum and is 0.33 (TW1), 0.40 (TI) and 0.44 (TW2). With an increase in the energy $E_{ex} > 13.4$ eV, the plateau is not observed, a small smooth decline in PLE-intensity begins at once.

PLE-peak (I) at 5.5 eV ($A_I = 0.4$) dominates in the low-energy region (4–10.5 eV) of all PLE-spectra. Another PLE-peak (II) is located at 6.2 eV, its amplitude depends on the type (TI, TW1 or TW2) of the spectrum. PLE-peak (II) almost completely overlaps with the PLE-peak (I), and amplitude $A_{II} = 0.25$ for all spectra recorded monitoring emission at $E_m = 3.1$ eV. The other spectrum ($E_m = 3.9$ eV) demonstrates the variations in $A_{II} = 0.15$ (TI), 0.30 (TW2) and 0.35 (TW1). In addition, small variations of PLE-intensity with an amplitude of less than 0.1 are observed in the energy region of 8.5–10.5 eV. Note that for $E_{ex} < 5$ eV, the PLE-intensity is 0.1–0.2, but this energy interval is already at the low-energy edge of the operating range for the setup #1.

PL under UV–Vis excitation was studied in the experimental setup #2. Figure 5 shows steady-state PL-emission spectra of LBAF10 crystal at $T = 80$ and 293 K recorded upon excitation in the vicinity of PLE-peak (I).

At $T = 80$ K the PL spectral shape depends on the excitation energy E_{ex}. In the case $E_{ex} = 4.4$ eV, a wide complex two-humped band with maxima at 2.35 and 2.75 eV (FWHM = 0.99 eV) dominates the PL emission spectrum. In the case $E_{ex} = 4.2$ eV, the dominant PL emission band exhibits only one maximum at 2.75 eV (FWHM = 0.74 eV). In both cases, variations in the PL intensity with an amplitude of less than 0.1 are observed in the energy region of 3.2–4.0 eV.

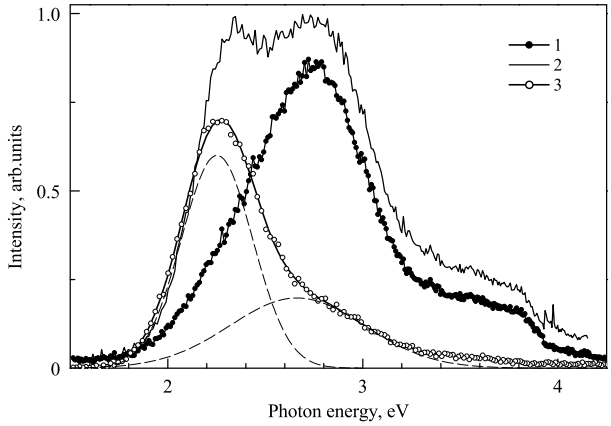

Figure 5: PL emission spectra of LBAF10 crystal at $T = 80$ (1, 2) and 293 K (3) recorded upon excitation at 4.2 (1), 4.4 (2), 5.2 eV (3). Spectrum (3): open circles are experimental data fitted by solid smooth curve; dashed Gaussians are principal constituents.

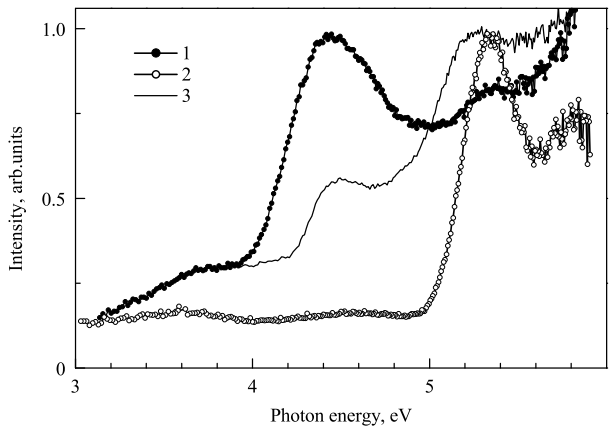

Figure 6: PLE spectra of LBAF10 crystal at $T = 80$ (1, 3) and 293 K (2) recorded monitoring emission at 2.23 (1), 2.29 (2), 2.78 eV (3).

At $T = 293$ K, the PL intensity is about 2/3 of that for 80 K. The change in the excitation energy E_{ex} affects mainly the PL intensity, while the spectrum shape varies little. The PL emission spectrum is represented by the dominant band at 2.27 eV (FWHM = 0.51 eV). The deconvolution of the PL emission spectrum revealed two main Gaussian-shape constituents: $E_{m1} = 2.25$ eV (FWHM = 0.43 eV) and $E_{m2} = 2.66$ eV (FWHM = 0.81 eV). The amplitude ratio is $A_{m2}/A_{m1} = 0.33$. Taking into account the expected temperature shift (about 0.1 eV), the values of E_{m1} and E_{m2} are comparable with the dominant maxima at 2.35 and 2.75 eV of the PL emission spectrum at 80 K.

Figure 6 shows normalized PLE-spectra of LBAF10 crystal at $T = 80$ and 293 K recorded monitoring emission at 2.2, 2.3 and 2.8 eV. At $T = 80$ K, the PLE-spectra in the energy range

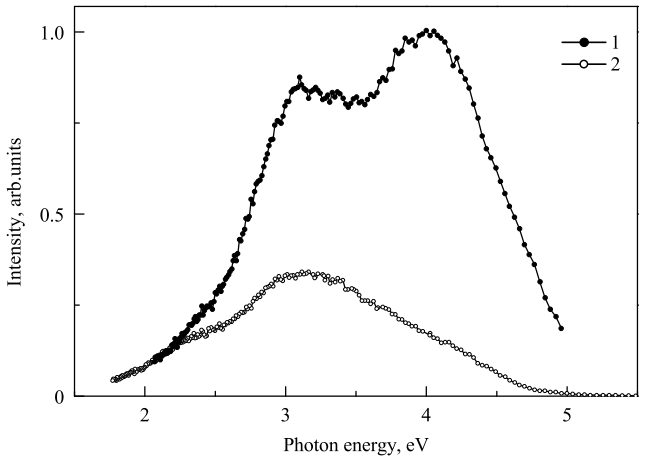

Figure 7: Normalized XRL-spectra of LBAF10 crystal at $T = 80$ (1) and 293 K (2) recorded upon excitation with X-ray tube at setup #2 (1) and X-ray synchrotron radiation at setup #3 (2).

of 3–6 eV consist of three main PLE-bands located at 3.6, 4.4 and 5.3 eV and differ only in the amplitudes of these bands. The PLE-bands at 4.4 ($E_m = 2.23$ eV) and 5.3 eV ($E_m = 2.78$ eV) are dominant. At $T = 293$ K, the PLE-spectrum is represented by one dominant narrow band at 5.35 eV.

3.3. XRL spectra

Figure 7 shows the luminescence spectra of LBAF10 crystal at $T = 80$ and 293 K recorded upon excitation by unfiltered X-ray radiation from an X-ray tube (setup #2) and from a synchrotron radiation source (setup #3). At 80 K, XRL-spectra are dominated by a luminescence band with a maximum at 4.1 eV, which partially overlaps with a less-intense band at about 3.2 eV. A low-intensity shoulder (2.0–2.5 eV) indicates a possible presence in this energy region of low-intensity partially overlapped luminescence bands. At 293 K, the XRL spectrum in the energy region of 1.5–6.2 eV can not be detected when excited by a laboratory source, since the XRL-intensity becomes too low. The X-ray radiation from a synchrotron source has an intensity many orders of magnitude greater than that of an X-ray tube. Therefore, the use of synchrotron radiation (setup #3) allowed us to register the XRL spectrum of LBAF10 crystal at 293 K. This spectrum is normalized in intensity arbitrarily for better viewing. The spectrum is dominated by a wide band at 3–3.2 eV, on the wings of which (2–2.2 eV and 4–4.5 eV) there can be observed relatively low-intensity shoulders.

3.4. Luminescence decay kinetics

Figure 8, *a* shows PL decay curves of LBAF10 crystal at $T = 8$ K recorded monitoring emission at $E_m = 3.1$ eV upon photoexcitation at $E_{ex} = 6.2$ and 12–15 eV. These curves are normalized in intensity. The PL decay kinetics can be represented as a superposition of an exponential component with a lifetime of 5.6 ns, a low-intensity component whose lifetime is commensurable with the TW2-window width, and the decay components of the micro- and millisecond time-range, which are manifested in our measurements as a constant level —

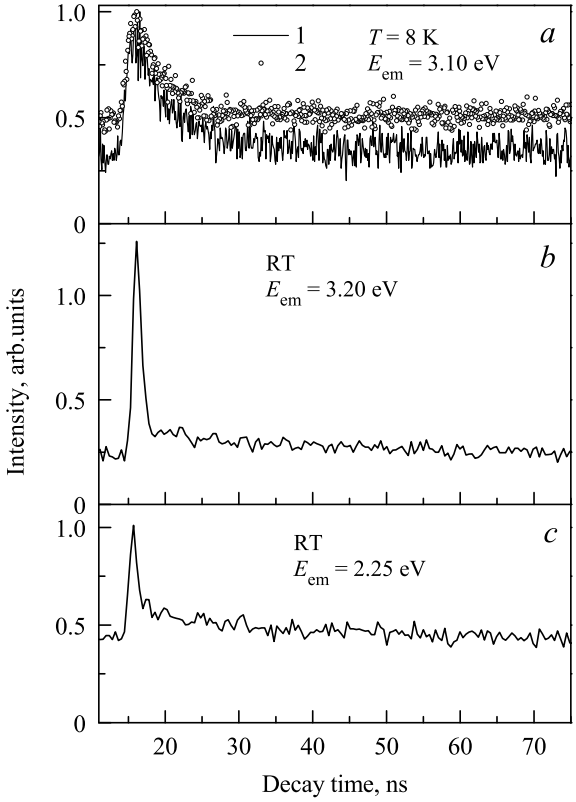

Figure 8: Luminescence decay kinetics of LBAF10 crystal at $T = 8$ (*a*) and 293 K (*b*, *c*) recorded monitoring emission at E_m upon photoexcitation (*a*) at $E_{ex} = 6.2$ (1) and 12–15 eV (2) or X-rays excitation (*b*, *c*). Panel *a*: each decay curve is divided by maximum of its intensity. Panels *b* and *c*: decay curves are divided by constant, so they are comparable in intensity.

pedestal. The PL decay curves in Fig. 8, *a* have the same value of lifetime ($\tau = 5.6$ ns), but differ in the pedestal level. In the case of $E_{ex} = 12$–15 eV, the contribution of inertial components is approximately 20 % greater.

In the case of $E_m = 3.9$ eV, the curves of PL decay kinetics were also recorded: they consist entirely of a pedestal, and the nanosecond exponential component is practically indistinguishable at the noise level. Therefore, such curves are not shown in Fig. 8, *a*.

The experimental data on PL decay kinetics make it possible to explain the differences between time-integrated and time-resolved PLE-spectra:

1. The shapes of PLE-spectra TI, TW1 and TW2 coincide in most cases, Fig. 4. This testifies to the prevailing contribution of the pedestal, i.e. the components of PL decay kinetics with a lifetime of micro- and millisecond time-ranges.

2. The normalized TI-spectrum looks like the average between the TW1 and TW2 spectra (for example, 13–21 eV in Fig. 4). This means a relatively small contribution of the pedestal and the prevalence of two nanosecond components: the first fast component ($\tau = 5.6$ ns) and the second component, whose lifetime is commensurate with the TW2-window width.

3. In some energy intervals, the normalized TI-spectrum demonstrates PLE-intensity, which is lower than that for TW1 and TW2. This is analogous to case 2 with an even smaller

contribution of the pedestal (for example, the energy regions of peaks (II) and (IV) in Fig. 4).

Figures 8, *b* and *c* show the curves of luminescence decay kinetics for LBAF10 crystal at $T = 293$ K recorded monitoring emission at E_m upon excitation with sub-nanosecond X-ray pulses of synchrotron radiation. Both curves (E_m= 2.25 and 3.20 eV) are qualitatively identical and consist of the fast subnanosecond decay component, which is dominant in intensity, a low-intensity exponential component with a lifetime of about 50 ns and a constant level — pedestal. The decay curves differ in the pedestal intensity and in the ratio of the intensities of the fast component and the pedestal. We note two opposite tendencies: a change from $E_m = 3.2$ eV to $E_m = 2.25$ eV leads to an increase in the pedestal intensity, while the relative intensity of the fast subnanosecond component decreases.

3.5. Thermoluminescence

Figure 9 shows TL glow curve of LBAF10 crystal recorded in the spectral-integral regime with linear heating rate of 0.3 K/s after X-ray irradiation at the initial temperature $T_0 = 90$ K. The TL glow curve was recorded in the temperature range of 90–500 K. However, Fig. 9 shows only its fragment for the temperature region of 90–360 K, since at 360–500 K the TL intensity does not exceed the noise level. The most intense TL glow peaks are labeled alphabetically from A to D. Two broad complex peaks at 140 (A) and 199 K (C) dominate in intensity (FWHM = 21.7 and 26.7 K). Two more relatively low-intensity peaks at 170 and 246 K are partially overlapped with the dominant peaks. The intensity of the peak (C) is taken as a conventional unit, the amplitudes of the other peaks are 0.75 (A) and about 0.1 (B and D).

The known TGCD-software [23] was used to deconvolute the TL glow curve in the temperature region of 100–360 K. Figure 9 shows both the deconvolution results achieved with FOM = 1.52 % and residual plot. From Fig. 9 it is seen that each dominant peak (A and C) consists of three less intense, partially overlapping peaks, whereas less intense experimental peaks B and D can be considered as single peaks. Table 3 shows the best-fit parameters for the eight deconvoluted peaks. From

Table 3: Best fit parameters for TL glow curve of LBAF10 crystal

Peak	T_m, K	A a.u.	ω, K	E, eV
	138.3	51.0	13.1	0.43
A	145.3	38.0	13.3	0.46
	153.3	19.0	13.7	0.50
B	170.4	14.0	12.7	0.67
	187.3	38.0	16.2	0.64
C	200.8	80.0	17.0	0.69
	209.0	31.0	16.3	0.73
D	247.3	16.0	16.1	0.77

Note. Peak is experimental TL glow peak (Fig. 9); parameters of the best-fit constituents: peak location (T_m), amplitude (A), FWHM (ω), activation energy (E).

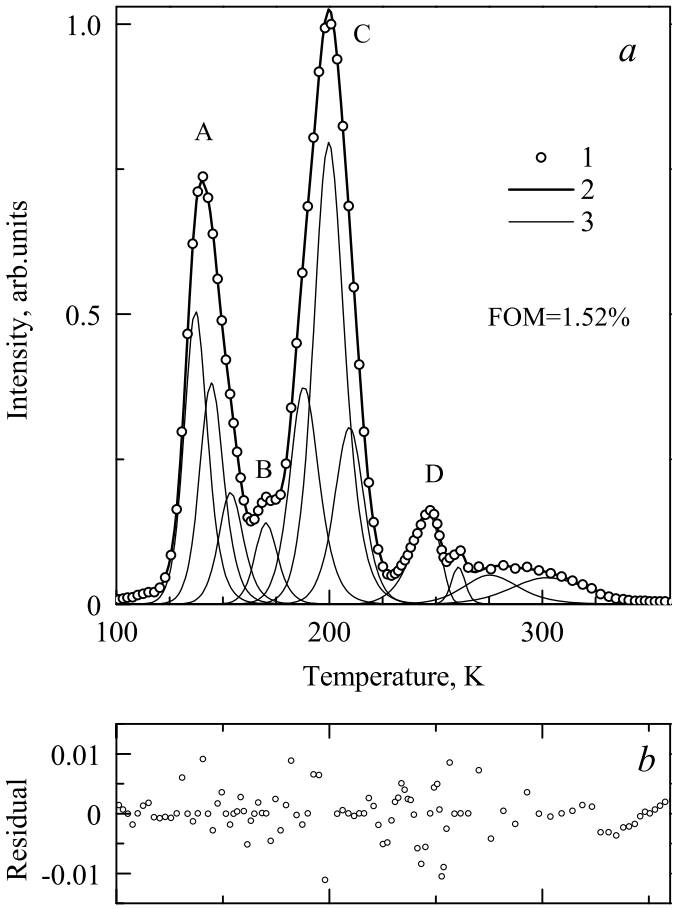

Figure 9: Panel *a*: TL glow curve of LBAF10 crystal ($T_0 = 90$ K) recorded in spectral-integral regime at linear heating rate of 0.3 K/s – (1), approximation curve – (2) and individual TL glow peaks – (3). Panel *b* shows Residual plot.

Tab. 3 it is seen that each of the TL glow peaks A and C is due to a superposition of at least three single peaks with similar thermal activation energies. This can indirectly indicate that in the temperature regions of the TL glow peaks A and C, there may be systems of traps with a discrete or continuous distribution over the activation energies.

It should be noted that the TL glow curve also contains several groups of extremely low-intensity, partially overlapping peaks at 100–120, 250–330 K. In deconvolution, their presence was taken into account by using five low-intensity virtual peaks, which were introduced from the condition of best convergence. However, the parameters of these five additional peaks can not be determined reliably, so they are not presented in Tab. 3.

3.6. Discussion

We are not aware of any published data on the electronic structure of the new compound — LBAF10 crystal. Therefore, we will determine some important electronic structure parameters from the experimental results obtained in this paper.

PL-excitation. The energy region of the dominant narrow PLE-peaks III and IV is classified as an excitonic region, i. e. energy region where direct creation of the lowest-energy excitons occurs. The PLE peak (III) is attributed to the creation of

near-defect excitons, whereas the PLE peak (IV) was interpreted as an intrinsic exciton peak. From contemporary representations (see, for example, [24, 25]) it follows that the shape of the lowest-energy PLE-peak (IV) associated with the creation of intrinsic excitons, is the result of two competing processes. The shape of the low-energy side of PLE-peak is due to an exponential increase in the host absorption, when E_{ex} increases at the low-energy tail of the host absorption region. The optical absorption increase leads to an increase in the number of electronic excitations created by light and, consequently, increases PL-intensity. The competing process consists in the fact that as the optical absorption increases, the distance to which light penetrates into the crystal decreases. In other words, there is a decrease in the volume of the region where it is possible to create electronic excitations. When the mean free path of created electronic excitations becomes commensurable with the distance to the surface, electronic excitations will reach the surface, and there will be nonradiative relaxation of them (surface energy losses, SEL). The maximum of the PLE-peak (IV) corresponds to the equality of the contributions of these two competing processes, and the high-energy side of the PLE-peak is determined by the second process (migration of electronic excitations to the surface accompanied by SEL). The intersection of the tangent to the low-energy slope of the PLE-peak (IV) and the abscissa axis gives an estimate of the cutoff point for the low-energy tail of the host-absorption $E_c = 11.2$ eV (Fig. 4), which in first approximation can be taken as the energy position of the low-energy edge of the LBAF10 host absorption. The E_c-energy thus determined corresponds to the energy threshold (E_{th}) for the excitation of STE-luminescence in LBAF10 crystal. With this interpretation, obviously, the following relation must be satisfied

$$E_{th} \approx E_c < E_{IV} < E_{n=1} < E_g,$$

here the conventional notations are used: $E_{n=1}$ is the energy position of the lowest-energy excitonic absorption maximum ($n = 1$); E_g is the band-gap width.

Within the framework of the developed ideas, the termination of the decline in PLE-intensity and its increase in the energy range from $E_{ex} = 13.0$ eV to E_V is due to the start of the lowest-energy band-to-band transitions, i. e. electronic transitions between the valence band (VB) top and the conduction band (CB) bottom. As an estimate of the band-gap width, we can take the value $E_g \approx 13.0$ eV (Fig. 4).

Obviously, these estimates can not replace any more direct measurements of the electronic structure parameters. However, in the absence of such data, indirect estimates are very useful, so they are summarized in Tab. 4.

PL-emission. Excitation in the exciton region at low temperatures leads to the appearance of the dominant Gaussian-shaped broad band at 4.0 eV (FWHM ≈ 1.4 eV) with a Stokes shift of about 6.7 eV, Fig. 3. The set of experimental data obtained does not contradict the assumption that the PL emission band is due to the radiative annihilation self-trapped excitons (STE) in LBAF10 crystal. We list the most characteristic features of the broadband UV luminescence at 4.0 eV in

Table 4: Electronic structure parameters (eV) of LBAF10 crystal derived from the luminescence spectroscopy results

Band gap width E_g	13.0
Energy interval, where the maximum of the lowest-energy excitonic absorption peak ($E_{n=1}$) is expected	11.72–13
Dominant PLE-maximum E_{IV}	11.72
Energy threshold for the excitation of STE-emission E_{th}	11.2
Low-energy onset of the intrinsic host absorption E_c	11.2
Dominant defect-relayed PLE-maximum E_{III}	11.25
Peak position and (FWHM) for STE emission	4.0 (1.4)
Energy position for the main defect relayed PL-band	3.0–3.2

LBAF10 crystal: the dominant band with a high quantum yield; the large Stokes shift; the absence of selective PLE-bands in the optical transparency region; the presence of an exponential component in the luminescence decay kinetics; the efficient excitation in the excitonic energy region; the freezing of efficient energy transfer to lattice defects. As is known, such a set of properties is possessed by STE in alkali-halide crystals (AHC) [26, 27], wide-band low-symmetry oxides (for example, in BeO [28, 29] and Al_2O_3 [30]), or in complex fluorides (for example, in $LiCaAlF_6$ [10, 11], $LiSrAlF_6$ [9, 10], $LiBaAlF_6$ [14, 31] and Li_3AlF_6 [17, 18]). This suggests that the broad dominant UV luminescence band in LBAF10 crystal is due to radiative annihilation of relaxed electronic excitations — self-trapped excitons, the decay of which leads to luminescence at 4.0 eV. The high excitation efficiency for this luminescence directly at the low-energy tail of the host absorption energy range indicates that these STEs are created as a result of the relaxation of intrinsic excitons e°.

PL emission band at 3.0–3.2 eV is the next band in descending order in intensity. It is located at the low-energy slope of the dominant PL emission band and overlaps with it. In this connection, the parameters of PL emission band at 3.0–3.2 eV can be determined only very approximately, its amplitude is estimated as 0.1–0.15 of that for the dominant band. The PL emission band at 3.0–3.2 eV should be attributed to luminescence of near-defect excitons. Indeed, the most efficient excitation of this luminescence occurs in the excitonic energy region: the PLE-peak at $E_{III} = 11.25$ eV. The spectroscopic parameters of the PLE peak (III) are close to those of the main excitonic PLE-peak (IV). In our opinion, the narrow intense PLE-peak (III) (Fig. 4) is due to the creation of excitons in the vicinity of unidentified lattice defects in LBAF10. At this stage, we can only make some assumptions about the nature of these defects. In particular, an elevated PLE-efficiency in the energy region of the low-energy tail of the host absorption suggests that we are not dealing with impurity defects, but rather the crystallographically nonequivalent lattice structural units resulting from its disordering. The near-defect excitons created in the energy region of PLE-peak (III) relax to the lowest excited state and their radiative annihilation in this structural unit determines the PL emission band at 3.0–3.2 eV. From the PLE-spectra it follows that there are at least two other channels of energy transfer of electronic excitations involving these defects. First, the pres-

ence of the PLE peak (IV) in the PLE spectrum at 3.0–3.2 eV indicates that there is also an effective excitonic energy transfer channel from the host lattice to these defect complexes. In other words, there is an energy transfer through migration of intrinsic excitons to the defects that results in the excitation of PL emission at 3.0–3.2 eV. Secondly, the presence of the PLE peak (III) in the PL excitation spectrum recorded monitoring emission at 4.0 eV indicates that after a direct creation of a near-defect exciton, its relaxation can be possible with transfer of energy to the defect-free region, which results in excitation of PL emission at 4.0 eV. Note that such a situation is not unique, similar energy transfer schemes are possible in other crystals, for example, in SrI_2:Nd^{3+} crystal [32].

In addition to the two main PL emission bands discussed above, we observed several low-intensity PL bands at 2.4–2.8, 3.5, and 4.5 eV. The amplitudes of all these bands do not exceed 0.1, they are efficiently excited in the crystal transparency region (PLE bands at 4.5, 5.3 and 6.2 eV). We attribute them to unidentified lattice defects (intrinsic or impurity-related) in LBAF10 crystal, the elucidation of the nature of which requires a separate study.

Band-to-band excitation. We shall analyze the experimental results for the energy region of $E_{ex} > E_g$ from a rather general view of the creation of excitons and separated charge carriers, i. e. free electrons and holes. From the point of view of the phenomena under consideration, the creation of a mobile exciton in this energy region leads to two main competing processes: (i) the exciton relaxation to the STE-state with subsequent radiative annihilation (PL emission band at 4.0 eV) and (ii) migration of the exciton to the surface with subsequent nonradiative relaxation, i. e. surface energy losses, SEL. The ratio of the contributions of these competing processes determines the PLE-intensity in the energy range of $E_{ex} > E_g$. Crystals with high-mobility electronic excitations (excitons) have a predominant second process and, respectively, in the energy range of $E_{ex} > E_g$, the PLE-efficiency is extremely low. An example of such crystals are lithium borates [33]. From general considerations it is obvious that an increase in the exciton mobility with an increase in E_{ex} should lead to a decrease in the PLE-intensity. This explains the gradual decrease in PLE-intensity, which is observed in Fig. 4, *a* at $E_{ex} > 18$ eV and in Fig. 4, *b* at $E_{ex} > 13$ eV.

The process of photo creation of separated electrons and holes is classified into several stages depending on the value $E_{ex} > E_g$. The lowest-energy electronic transitions with energy E_{ex}, which only slightly exceed E_g, lead to the creation of an electron-hole pair in which the hole is at the states of the VB top. The electron is excited to the CB bottom, but is in the potential well due to the Coulomb potential of the hole. At zero energy ($E_{ex} \approx E_g$), the electron is at the CB bottom, but it can not overcome the Coulomb potential of hole barrier, which subsequently leads to recombination of the geminate pair or its relaxation to the STE-state with subsequent radiative annihilation. With an increase in the excitation energy $E_{ex} > E_g$, the electron receives sufficient energy to overcome the Coulomb potential barrier, but there is an energy interval in which the electron energy is already sufficient to overcome the potential barrier, but recombination predominantly proceeds in geminate pairs. During this energy interval, there are no serious reasons for significant changes in PLE-efficiency. It is this process that explains the presence of a 'plateau' in the energy interval of 13–18 eV, Fig. 4, *a*. Here it should be noted that the luminescence spectrum recorded upon photoexcitation into the energy region of $E_{ex} = 18$–20 eV does not contain any new 'emission band' in the UV spectral region, Fig. 3. This E_{ex} energy corresponds to the excitation of 5 *p*-states of Ba^{2+} ions. From this result it follows that we did not succeed in registering Auger-free luminescence in LBAF10 crystals. It can be assumed that such a luminescence of LBAF10 in the UV/VUV region can be detected upon excitation with a high-power electron beam. A similar situation is realized in related $LiBaAlF_6$ crystals and was reported in our papers [14, 31].

Summarizing the discussion of the luminescence excitation process in the region of low-energy band-to-band transitions, we note that when the STE-luminescence is excited (Fig. 4, *a*), the contributions of the 'exciton' and 'recombination' mechanisms are comparable, whereas in the excitation of defect-related luminescence (Fig. 4, *b*) the 'exciton' mechanism prevails.

X-ray excitation leads, ultimately, to the appearance of relaxed free charge carriers thermalized to the levels of VB-top (holes) and CB-bottom (electrons). Then two main cases are possible. In the first case, when the free charge carriers are localized at local trapping centers after irradiation is terminate, we have a system of occupied trapping centers, the study of which by TL-technique gives an idea of the energy characteristics of certain trapping centers, Fig. 9. From Tab. 3 it is seen that in the temperature range of 90–350 K four TL glow peaks with activation energies from 0.46 to 0.77 eV are observed. In the second case, a radiative recombination of the free charge carriers with charge carriers of the opposite sign localized at the recombination centers takes place resulting in XRL. The steady-state XRL-spectra (Fig. 7) give an idea of the recombination luminescence spectrum of LBAF10. At $T = 80$ K, both characteristic bands at 3.0–3.2 and 4.0 eV are present in the recombination luminescence spectrum. This agrees well with the previous conclusion about their efficient photoexcitation at $E_{ex} > E_g$. At room temperature, the defect-related luminescence dominates in the XRL-spectrum, which also agrees with the previous conclusion about the low-temperature character of the STE-luminescence in LBAF10.

4. Conclusions

A new wide bandgap optical material — noncentrosymmetric $Li_2BaAl_2F_{10}$ (LBAF10) single crystal — has been reported in the present research work. An overview of all available literature did not give any other reports on LBAF10, so it can be considered as a novel optical material. This research paper reports a large amount of primary data relating to the crystallographic structure of LBAF10, their luminescence properties and electronic structure parameters.

The vertical Bridgman method is proved to be fairly suitable for growing LBAF10 crystal ingot and subsequent preparation of single-crystal samples of optical quality suitable for spectroscopic studies.

The lack of reference literature data on LBAF10 crystallography forced us to apply the single crystal XRD method to identify the new optical material, and use a complex data-processing to determine its crystallographic structure (orthorhombic symmetry $Cmc2_1$), lattice parameters, and atomic coordinates.

Luminescent spectroscopy of LBAF10 was used both for the study of primary luminescence properties and for the experimental determination of certain parameters of its electronic structure. For this purpose, various types of excitations were used: (i) selective photoexcitation using synchrotron radiation ($T = 8$ K, time-resolved spectra) and discharge lamp light source; (ii) x-ray beam from both the synchrotron source and an X-ray tube. In addition to PL and PLE-spectra, the luminescence decay kinetics under synchrotron excitation of two types has been studied: selective photoexcitation and excitation by subnanosecond pulses of x-rays.

A low-temperature broadband luminescence at $E_m = 4.0$ eV ($E_{ex} = 11.72$ eV) is revealed, whose properties allow it to be attributed to radiative annihilation of self-trapped excitons.

A near-defect excitonic-type luminescence at $E_m = 3.0$–3.2 eV ($E_{ex} = 11.25$ eV) is revealed. The results obtained allow us to assume that the defect areas can be preliminarily associated with nonequivalent structural units or structural disordering of the crystal lattice.

The electronic structure parameters (bandgap $E_g = 13.0$ eV, low-energy onset of the intrinsic host absorption $E_c = 11.2$ eV); energy threshold for the excitation of STE-luminescence ($E_{th} = 11.2$ eV), energy interval (11.72–13.0 eV), where the lowest-energy excitonic absorption peak ($E_{n=1}$) is expected, are determined by luminescence spectroscopy methods.

Thermoluminescence study of LBAF10 revealed several few defects, which manifest themselves as four partially overlapping TL glow peaks in the temperature range of 90–350 K. The TL glow curve was decomposed using TGCD method, and the thermal activation parameters were determined. In particular, the activation energies of the revealed TL glow peaks are localized in the temperature range of 0.46–0.77 eV. However, a determination of the nature of the defects found requires a separate future study.

Acknowledgments

This work has been supported by the Ministry of Education and Science of the Russian Federation (basic part of the government mandate – Project № 3.8302.2017/8.9) and by State assignment (Project № 0330-2016-0008).

References

[1] W. Pies, A. Weiss, in: Key Elements: F, Cl, Br, I, Vol. 7a of Landolt-Börnstein - Group III Condensed Matter, Springer Berlin Heidelberg, 1973, pp.254–265.
[2] Ch. B. Lushchik, A. Ch. Lushchik, Decay of electronic excitations with defect formation in solids, Nauka, Moscow, 1989.
[3] C. V. Kannan, K. Shimamura, H. R. Zeng, H. Kimura, E. G. Villora, K. Kitamura, J. Appl.Phys. 104 (2008) 114113.
[4] E. G. Villora, K. Shimamura, K. Sumiya, H.Ishibashi, Opt. Expr. 17 (2009) 12362.
[5] M. J. Knitel, P. Dorenbos, J. T. M. de Haas, C. W. E. van Eijk, in: Proceedings of the International Conference on Inorganic Scintillators and Their Applications, Delft University Press, Delft, The Netherlands, 1995, pp.81–83.
[6] A. Meijerink, J. Lumin. 55 (3) (1993) 125.
[7] L. Prado, N. D. Vieira, Jr., S. P. Morato, and J. Y. Gesland, Solid State Commun. 87 (1) (1993) 41.
[8] L. Prado, N. D. Vieira, Jr., S. L. Baldochi, S. P. Morato, J. P. Deniss, N. Tercier, and B. Blanzat, J. Phys. Chem. Solids 57 (4) (1996) 413.
[9] M. True, M. Kirm, E. Negodine, S. Vielhauer, G. Zimmerer, J. Alloys Compd. 374 (1–2) (2004) 36.
[10] N. Shiran, A. Gektin, S. Neicheva, M. Weber, S. Derenzo, M. Kirm, M. True, I. Shpinkov, D. Spassky, K. Shimamura, N. Ichinose, Nucl. Instrum. Meth. Phys. Res. A 537 (2005) 266.
[11] M. Kirm, M. True, S. Vielhauer, G. Zimmerer, N. V. Shiran, I. Shpinkov, D. Spassky, K. Shimamura, N. Ichinose, Nucl. Instrum. Meth. Phys. Res. A 537 (2005) 291.
[12] S. I. Omelkov, M. Kirm, E. Feldbach, V. A. Pustovarov, S. O. Cholakh, and L. I. Isaenko, J. Phys.: Condens. Matter. 22 (29) (2010) 295504(8).
[13] I. N. Ogorodnikov, S. I. Omelkov, V. A. Pustovarov, A. Kasikov, and M. Kirm, Opt. Mater. 39 (2015) 52.
[14] V. A. Pustovarov, I. N. Ogorodnikov, S. I. Omelkov, D. A. Spassky, and L. I. Isaenko, J. Opt. Soc. Am. B-Opt. Physics 31 (8) (2014) 1926.
[15] S. I. Omelkov, V. Kiisk, I. Sildos, M. Kirm, V. Nagirnyi, V. A. Pustovarov, L. I. Isaenko, and S. I. Lobanov, Radiat. Meas. 56 (2013) 49.
[16] I. N. Ogorodnikov, V. A. Pustovarov, S. I. Omelkov, M. Kirm, Opt. Mater. 69 (2017) 344.
[17] V. A. Pustovarov, I. N. Ogorodnikov, S. I. Omelkov, M. S. Molokeev, A. V. Kozlov, L. I. Isaenko, Opt. Mater. 49 (2015) 201.
[18] V. A. Pustovarov, I. N. Ogorodnikov, S. I. Omelkov, L. I. Isaenko, Radiat. Meas. 90 (2016) 51.
[19] G. Zimmerer, Radiat. Meas. 42 (4–5) (2007) 859.
[20] V. A. Pustovarov, E. I. Zinin, A. L. Krymov, B. V. Shulgin, Rev. Scient. Instrum. 63 (1992) 3521.
[21] N. E. Kashcheeva, D. Yu. Naumov, E. V. Boldyreva, Z. Kristallog. 214 (9) (1999) 534.
[22] P. Muller, R. Herbst-Irmer, A. L. Spek, T. R. Schneider, M. R. Sawaya, Crystal Structure Refinement. A Crystallographer's guide to SHELXL, Oxford University Press, New York, 2006.
[23] J. Peng, Z. Dong, F. Han, SoftwareX 5 (2016) 112.
[24] A. N. Vasil'ev, V. V. Mikhailin, Introduction in Solid State Spectroscopy, Moscow University Press, Moscow, 1987.
[25] T. Matsumoto, M. Shirai, K. Kan'no, J. Phys. Soc. Jpn. 64 (3) (1995) 987.
[26] Ch. B. Lushchik, Free and self-trapped excitons in alkali halides: Spectra and dynamics, in: Excitons, Publ. Conf., Amsterdam, North-Holland, 1982, pp.506–541.
[27] A. K. S. Song, R. T. Williams, Self-Trapped Excitons, Springer-Verlag, Berlin-Heidelberg, New York, 1996.
[28] I. N. Ogorodnikov, V. Yu. Ivanov, A. V. Kruzhalov, Phys. Solid State 36 (11) (1994) 1748.
[29] V. A. Pustovarov, V. Yu. Ivanov, M. Kirm, A. V. Kruzhalov, A. V. Korotaev, G. Zimmerer, Phys. Solid State 43 (7) (2001) 1233.
[30] B. R. Namozov, M. É. Fominich, R. I. Zakharchenya, V. V. Myurk, Phys. Solid State 40 (5) (1998) 837.
[31] I. N. Ogorodnikov, S. I. Omelkov, V. A. Pustovarov, A. Kasikov, M. Kirm, Opt. Mater. 39 (2015) 52.
[32] I. N. Ogorodnikov, V. A. Pustovarov, A. A. Goloshumova, L. I. Isaenko, A. P. Yelisseyev, V. M. Pashkov, J. Lumin. 143 (2013) 101.
[33] I. N. Ogorodnikov, V. A. Pustovarov, A. V. Kruzhalov, L. I. Isaenko, M. Kirm, G. Zimmerer, Phys. Solid State 42 (3) (2000) 464.